Crystal field analysis of Dy and Tm implanted silicon for photonic and quantum technologies

Mark A. Hughes,[1,*] Manon A. Lourenço,[1] J. David Carey,[1,2] Ben Murdin[1] and Kevin P. Homewood[1]

[1]*Advanced Technology Institute, University of Surrey, Guildford, GU2 7XH, United Kingdom*
[2]*Department of Electronic Engineering, University of Surrey, Guildford, GU2 7XH, United Kingdom*
[*]*m.a.hughes@surrey.ac.uk*

Abstract: We report the lattice site and symmetry of optically active Dy^{3+} and Tm^{3+} implanted Si. Local symmetry was determined by fitting crystal field parameters (CFPs), corresponding to various common symmetries, to the ground state splitting determined by photoluminescence measurements. These CFP values were then used to calculate the splitting of every J manifold. We find that both Dy and Tm ions are in a Si substitution site with local tetragonal symmetry. Knowledge of rare-earth ion symmetry is important in maximising the number of optically active centres and for quantum technology applications where local symmetry can be used to control decoherence.

OCIS codes: (160.2540) Fluorescent and luminescent materials; (160.6000) Semiconductor materials.

References and links

1. W. L. Ng, M. A. Lourenco, R. M. Gwilliam, S. Ledain, G. Shao, and K. P. Homewood, "An efficient room-temperature silicon-based light-emitting diode," Nature **410**, 192-194 (2001).
2. M. A. Lourenço, R. M. Gwilliam, and K. P. Homewood, "Silicon light emitting diodes emitting over the 1.2-1.4 μm wavelength region in the extended optical communication band," Appl. Phys. Lett. **92**(2008).
3. M. A. Lourenço, Z. Mustafa, W. Ludurczak, L. Wong, R. M. Gwilliam, and K. P. Homewood, "High temperature luminescence of Dy^{3+} in crystalline silicon in the optical communication and eye-safe spectral regions," Opt. Lett. **38**, 3669-3672 (2013).
4. M. A. Hughes, R. J. Curry, and D. W. Hewak, "Determination of the oxidation state and coordination of a vanadium doped chalcogenide glass," Opt. Mater. **33**, 315–322 (2011).
5. M. A. Hughes, R. J. Curry, and D. W. Hewak, "Spectroscopy of titanium-doped gallium lanthanum sulfide glass," J. Opt. Soc. Am. B-Opt. Phys. **25**, 1458-1465 (2008).
6. M. A. Hughes, T. Akada, T. Suzuki, Y. Ohishi, and D. W. Hewak, "Ultrabroad emission from a bismuth doped chalcogenide glass," Opt. Express **17**, 19345-19355 (2009).
7. M. A. Hughes, R. M. Gwilliam, K. Homewood, B. Gholipour, D. W. Hewak, T.-H. Lee, S. R. Elliott, T. Suzuki, Y. Ohishi, T. Kohoutek, and R. J. Curry, "On the analogy between photoluminescence and carrier-type reversal in Bi- and Pb-doped glasses," Opt. Express **21**, 8101-8115 (2013).
8. D. L. Adler, D. C. Jacobson, D. J. Eaglesham, M. A. Marcus, J. L. Benton, J. M. Poate, and P. H. Citrin, "Local structure of 1.54 μm luminescence Er^{3+} implanted in Si," Appl. Phys. Lett. **61**, 2181-2183 (1992).
9. F. Priolo, G. Franzò, S. Coffa, A. Polman, S. Libertino, R. Barklie, and D. Carey, "The erbium‐impurity interaction and its effects on the 1.54 μm luminescence of Er^{3+} in crystalline silicon," J. Appl. Phys. **78**, 3874-3882 (1995).
10. A. Kozanecki, R. J. Wilson, B. J. Sealy, J. Kaczanowski, and L. Nowicki, "Evidence of interstitial location of Er atoms implanted into silicon," Appl. Phys. Lett. **67**, 1847-1849 (1995).
11. J. S. Custer, A. Polman, and H. M. van Pinxteren, "Erbium in crystal silicon: Segregation and trapping during solid phase epitaxy of amorphous silicon," J. Appl. Phys. **75**, 2809-2817 (1994).
12. Y. S. Tang, J. Zhang, K. C. Heasman, and B. J. Sealy, "Lattice locations of erbium implants in silicon," Solid State Commun. **72**, 991-993 (1989).
13. J. D. Carey, J. F. Donegan, R. C. Barklie, F. Priolo, G. Franzò, and S. Coffa, "Electron paramagnetic resonance of erbium doped silicon," Appl. Phys. Lett. **69**, 3854-3856 (1996).
14. J. D. Carey, R. C. Barklie, J. F. Donegan, F. Priolo, G. Franzo, and S. Coffa, "Electron paramagnetic resonance and photoluminescence study of Er-impurity complexes in Si," Phys. Rev. B **59**, 2773-2782 (1999).

15. U. Wahl, A. Vantomme, J. De Wachter, R. Moons, G. Langouche, J. G. Marques, J. G. Correia, and I. Collaboration, "Direct evidence for tetrahedral interstitial Er in Si," Phys. Rev. Lett. **79**, 2069-2072 (1997).
16. M. Needels, M. Schlüter, and M. Lannoo, "Erbium point defects in silicon," Phys. Rev. B **47**, 15533-15536 (1993).
17. T. Böttger, C. W. Thiel, R. L. Cone, and Y. Sun, "Effects of magnetic field orientation on optical decoherence in Er^{3+}:Y_2SiO_5," Phys. Rev. B **79**, 115104 (2009).
18. K. Saeedi, S. Simmons, J. Z. Salvail, P. Dluhy, H. Riemann, N. V. Abrosimov, P. Becker, H.-J. Pohl, J. J. L. Morton, and M. L. W. Thewalt, "Room-temperature quantum bit storage exceeding 39 minutes using ionized donors in silicon-28," Science **342**, 830-833 (2013).
19. T. Miyamachi, T. Schuh, T. Markl, C. Bresch, T. Balashov, A. Stohr, C. Karlewski, S. Andre, M. Marthaler, M. Hoffmann, M. Geilhufe, S. Ostanin, W. Hergert, I. Mertig, G. Schon, A. Ernst, and W. Wulfhekel, "Stabilizing the magnetic moment of single holmium atoms by symmetry," Nature **503**, 242-246 (2013).
20. P. Pichler, *Intrinsic Point Defects, Impurities, and Their Diffusion in Silicon* (Springer, 2004).
21. J. J. Baldovi, S. Cardona-Serra, J. M. Clemente-Juan, E. Coronado, A. Gaita-Arino, and A. Palii, "Rational design of single-ion magnets and spin qubits based on mononuclear lanthanoid complexes," Inorg. Chem. **51**, 12565-12574 (2012).
22. S. Bertaina, S. Gambarelli, A. Tkachuk, I. N. Kurkin, B. Malkin, A. Stepanov, and B. Barbara, "Rare-earth solid-state qubits," Nat. Nanotechnol. **2**, 39-42 (2007).
23. I. D. Abella, N. A. Kurnit, and S. R. Hartmann, "Photon echoes," Phys.Rev. **141**, 391-& (1966).
24. R. M. Macfarlane, "Photon-echo measurements on the trivalent thulium ion," Opt. Lett. **18**, 1958-1960 (1993).
25. J. B. Gruber, B. Zandi, and L. Merkle, "Crystal-field splitting of energy levels of rare-earth ions $Dy^{3+}(4f^9)$ and $Yb^{3+}(4f^{13})$ in M(II) sites in the fluorapatite crystal $Sr_5(PO_4)_3F$," J. Appl. Phys. **83**, 1009-1017 (1998).
26. U. Walter, "Treating crystal field parameters in lower than cubic symmetries," J. Phys. Chem. Solids **45**, 401-408 (1984).
27. M. Lourenco, R. Gwilliam, and K. Homewood, "Eye-safe 2 μm luminescence from thulium-doped silicon," Opt. Lett. **36**, 169-171 (2011).
28. D. S. Pytalev, S. A. Klimin, and M. N. Popova, "Optical high-resolution spectroscopic study of Tm^{3+} crystal-field levels in $LiLuF_4$," J. Rare Earth **27**, 624-626 (2009).
29. H. P. Jenssen, A. Linz, R. P. Leavitt, C. A. Morrison, and D. E. Wortman, "Analysis of the optical spectrum of Tm^{3+} in $LiYF_4$," Phys. Rev. B **11**, 92-101 (1975).
30. B. G. Wybourne and L. Smentek, *Optical Spectroscopy of Lanthanides: Magnetic and Hyperfine Interactions* (Taylor & Francis, 2007).
31. D. J. Newman and B. Ng, *Crystal Field Handbook* (Cambridge University, 2007).
32. J. Mulak and M. Mulak, "Capability of the free-ion eigenstates for crystal-field splitting," J. Mod. Phys. **2**, 1373-1389 (2011).
33. K. R. Lea, M. J. M. Leask, and W. P. Wolf, "The raising of angular momentum degeneracy of f-electron terms by cubic crystal fields," J. Phys. Chem. Solids **23**, 1381-1405 (1962).
34. S. Edvardsson and D. Aberg, "An atomic program for energy levels of equivalent electrons: lanthanides and actinides," Comput. Phys. Commun. **133**, 396-406 (2001).
35. W. T. Carnall, G. L. Goodman, K. Rajnak, and R. S. Rana, "A systematic analysis of the spectra of the lanthanides doped into single crystal LaF_3," The Journal of Chemical Physics **90**, 3443-3457 (1989).
36. D. J. Newman and B. Ng, "The superposition model of crystal fields," Rep. Prog. Phys. **52**, 699 (1989).
37. J. J. Baldovi, S. Cardona-Serra, J. M. Clemente-Juan, E. Coronado, A. Gaita-Arino, and A. Palii, "SIMPRE: A software package to calculate crystal field parameters, energy levels, and magnetic properties on mononuclear lanthanoid complexes based on charge distributions," J. Comput. Chem. **34**, 1961-1967 (2013).
38. J. J. Baldoví, J. M. Clemente-Juan, E. Coronado, A. Gaita-Ariño, and A. Palii, "An updated version of the computational package SIMPRE that uses the standard conventions for Stevens crystal field parameters," J. Comput. Chem. **35**, 1930-1934 (2014).
39. J. Mulak and Z. Gajek, *The Effective Crystal Field Potential* (Elsevier, 2000).
40. M. Faucher and D. Garcia, "Crystal field effects on 4f electrons: Theories and reality," J. Less-Common Met. **93**, 31-44 (1983).
41. J. J. Baldovi, J. J. Borras-Almenar, J. M. Clemente-Juan, E. Coronado, and A. Gaita-Arino, "Modelling the properties of lanthanoid single-ion magnets using an effective point-charge approach," Dalton Trans. **41**, 13705-13710 (2012).
42. P. Pal, T. Penhouet, V. D'Anna, and H. Hagemann, "Effect of pressure on the free ion and crystal field parameters of Sm^{2+} in BaFBr and SrFBr hosts," J. Lumines. **134**, 678-685 (2013).
43. P. Vogl, "Dynamical effective charges in semiconductors: A pseudopotential approach," J. Phys. D-Solid State **11**, 251 (1978).
44. A. V. Larin and D. P. Vercauteren, "Approximation of Mulliken charges for the silicon atoms of all-siliceous zeolites," Int. J. Inorg. Mater. **1**, 201-207 (1999).
45. M. Milosavljević, G. Shao, M. A. Lourenco, R. M. Gwilliam, and K. P. Homewood, "Engineering of boron-induced dislocation loops for efficient room-temperature silicon light-emitting diodes," J. Appl. Phys. **97**, 073512 (2005).

46. M. A. Lourenço, M. Milosavljević, G. Shao, R. M. Gwilliam, and K. P. Homewood, "Boron engineered dislocation loops for efficient room temperature silicon light emitting diodes," Thin Solid Films **504**, 36-40 (2006).

1. Introduction

Silicon is unprecedented in its technological applications, however, its indirect electronic band gap makes it a poor light emitter due to fast non-radiative decay dominating over slower radiative routes, which limits its photonic applications. Dislocation engineering by boron implantation can be used to inhibit non-radiative decay paths and allow band edge photoluminescence (PL) and electroluminescence (EL) from Si [1]. The same dislocation engineering technique, accompanied by rare-earth (RE) implantation can be used to obtain PL and EL at specific wavelengths determined by the RE optical transitions [2, 3]. As a consequence, RE implanted Si is a promising platform for future photonic applications. However, comparatively little is known about the local environment of optically active RE ions implanted into silicon, which limits the optimisation of this technology. The atomic shielding of the *f*-shell electrons in REs means that the effect of the host crystal field on their energy levels is weaker when compared with transition metal ions [4, 5] or bismuth [6, 7]. Nevertheless, the complex *f*-shell inter-electron (coulomb) and spin-orbit interactions, along with the simultaneous influence of the crystal field, give rise to intricate energy level splitting that is highly dependent on the local crystal field environment of the RE and can reveal detailed structural information. Because of the low number of optically active ions in implanted samples compared to bulk doped samples, measuring the crystal field splitting from absorption measurements in implanted samples is extremely difficult. PL spectra can often be detected, but are inherently weak because above band gap excitation is required, and this only penetrates the first few hundred nm from the sample's surface. Therefore, various peaks in the crystal field split spectra can be undetected or unresolved.

Er implanted Si has been investigated extensively in comparison to other REs, largely because of the telecoms applications of its 1.5 μm luminescence. Extended X-ray absorption fine structure (EXAFS) measurements of Er-implanted, high O impurity Czochralski-grown Si, which exhibit strong PL at 1.54 μm, show Er is six-fold coordinated to oxygen [8]. Strong PL can also be observed from Er and O coimplanted Si [9]. By contrast, in low O impurity FZ Si, no PL was observed and Er was coordinated with 12 Si atoms [8]. Contradictory Rutherford backscattering (RBS) measurements have indicated that Er implanted in Si is located [10], and is not located [11], at an interstitial site. Other RBS and PL measurements indicate that when annealed at over 800°C, 80% of Er occupies substitutional sites with tetrahedral symmetry [12]. Electron paramagnetic resonance (EPR) spectra of Er and O coimplanted Si indicate two Er^{3+} centers having monoclinic C_{1h} symmetry [13] and trigonal symmetry [14]. The emission channelling technique indicates that Er in FZ Si occupies tetrahedral interstitial sites [15], and first-principles calculations indicate that the lowest energy configuration of Er in Si is Er^{3+} at a tetrahedral interstitial site [16]. These contradictory experimental findings on the local structure of Er in Si indicate that processing and annealing conditions have a strong influence in the local environment of Er implanted into Si. It is therefore highly likely that processing conditions can influence the local environment of other REs implanted into Si.

RE ions are also ideal systems for quantum technologies because the shielding of their *f*-shell electrons offers an atomic scale barrier to decoherence. Long decoherence times, up to 4 ms, for internal RE transitions have been demonstrated in RE doped optical crystals [17]. Major sources of decoherence arise from the interaction with the nuclear spin or from the thermal bath of electrons of the host. Silicon has an inherently low nuclear spin, and isotopically pure silicon has zero nuclear spin. Recently, a room temperature decoherence

time of 39 min has been demonstrated for phosphorous impurites in isotopically pure ^{28}Si [18]. Combining the shielding of RE *f*-electrons with the low nuclear spin and processing pedigree of silicon offers a novel system in which to implement quantum technologies. Since the decoherence of RE quantum states is strongly influenced by the crystal field and nuclear spin of its local environment, knowledge and control of this environment is critical for the implementation of quantum technologies based on RE implanted Si.

The symmetry of the RE ion local environment is particularly important for RE quantum states, for example the magnetic moment of single neutral Ho atoms on a platinum substrate has been shown to have lifetimes of the order of minutes, which could be useful for the storage of qubits [19]. This long lifetime was explained because in the particular case of total angular momentum ,J, = 8 for Ho and the C_{3v} symmetry of the Pt <111> substrate, the eigenstates of the crystal field Hamiltonian form three distinctive groups which can be used to show that the matrix elements describing a substrate electron-induced transition between degenerate m_J magnetic sublevels vanish. This means the Ho atoms are in effect invisible to the electrons moving through the Pt. Any RE atom with J = 3n + 1 or 3n +2, for any interger n $\geq$ 0, should also show long lifetimes; this leaves only Pr and Pm, the later having no stable isotopes [19]. C_{3v} symmetry can occur for substitutional impurities in Si if there is distortion in the <111> direction, or if a pair of inequivalent substitutional atoms are bonded [20]. In other work relating the symmetry of REs to their applications in quantum technologies, it has been shown that increasing the ground state tunnelling gap of RE complexes can minimise decoherence from nuclear spins [21]. The design of RE systems with large tunnelling gaps requires an m_J ground state doublet that can mix with off-diagonal crystal field parameters allowed by the below cubic symmetry of the RE; such symmetries include D_{4d} [21]. Since the implantation and post implant annealing conditions for Er implanted Si can give rise to different symmetries for Er, it may be possible to engineer a RE implanted Si system with a symmetry that stabilizes the magnetic moment, for example Pr or Ho with C_{3v} symmetry, or decreases decoherence from nuclear spins, for example Tb or Ho with D_{4d} symmetry, by optimising the processing conditions. This would require a method to rapidly determine the symmetry of the sample, such as analysing the PL from the sample, which would allow the development of processing conditions which produce a RE symmetry favorable for quantum technology applications.

The usefulness of RE doped materials for quantum technologies can be determined by measuring the spin decoherence time using spin echo [22], or the optical decoherence time using photon echo [23]. Tm and Dy doped materials have received little attention for quantum technology applications compared to other REs. Photon echo measurements of Tm^{3+} doped LaF_3 and YAG revealed zero field decoherence times of 7 and 75μs, respectively [24]. The magnetic field dependence and nonexponential character of the echo decays indicated that decoherence was due to nuclear spin fluctuations of the host [24]. Since silicon, and in particular isotopically pure ^{28}Si, have low nuclear spin we expect the decoherence time to be significantly improved in Tm implanted Si. In this work we report for the first time crystal field analysis of the PL from Dy and Tm ions implanted into Si which is used to determine symmetry and structural parameters. Our analysis method could be used as a quick technique to screen the processing conditions of optically active RE implanted into Si, which would be useful for the development of quantum and photonic technologies based on RE implanted Si.

2. Experimental

Dy and Tm implanted Si samples were fabricated by room temperature Dy or Tm implantation (10^{13} ion/cm^2 at 400 keV) into n-type Si <100> substrates (2–7 Ωcm) previously implanted with B at an energy of 30 keV and a dose of 10^{15} ion/cm^2. The samples were then annealed in N_2 ambient at 850°C for 5 min. Photoluminescence (PL) measurements were obtained by placing the samples in a continuous flow liquid nitrogen cryostat at 80 K.

Samples were excited by a 532 nm diode-pumped laser line at a power density of ~0.3 W/cm^2, optical emission was dispersed with a monochromator and detected with an extended InGaAs detector using standard phase sensitive detection.

3. Results and discussion

3.1 Photoluminescence measurements

We show the PL spectra of Dy and Tm implanted Si in Figs. 1 and 2, respectively. In each case we overlapped PL spectra corresponding to transitions from multiple J manifolds to the ground state to reduce uncertainty in the position of energy levels in the ground state. For Dy^{3+} ($4f^9$) the quantum numbers of the ground state are S = 5/2, L = 5 and J = 15/2, for Tm^{3+} ($4f^{12}$) they are S = 1, L = 5 and J = 6.

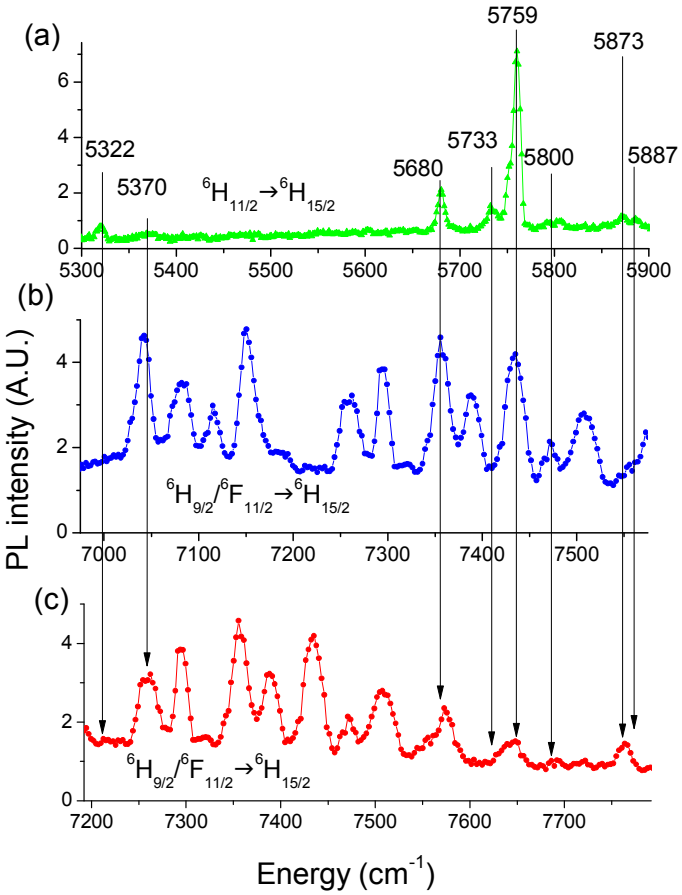

Fig. 1 PL spectra of Dy implanted Si excited at 532 nm. The $^6H_{11/2} \rightarrow {}^6H_{15/2}$ transition is shown in (a), the $^6H_{9/2} \rightarrow {}^6H_{15/2}$ and $^6F_{11/2} \rightarrow {}^6H_{15/2}$ mixture of transitions are shown in (b) and (c). To align the transition energy scale, (b) is offset from (a) by 1675 cm^{-1}, and (c) is offset from (b) by 216 cm^{-1}. Peaks identified as corresponding to splitting of the $^6H_{15/2}$ ground state are identified with arrows, along with the energy of the peaks.

The PL spectra for Dy implanted Si in the 7000 to 7800 cm^{-1} region contains a mixture of $^6H_{9/2} \rightarrow {}^6H_{15/2}$ and $^6F_{11/2} \rightarrow {}^6H_{15/2}$ transitions [3], which is caused by overlapping of the $^6H_{9/2}$ and $^6F_{11/2}$ manifolds [25]. This makes determination of the ground state splitting difficult, however, the 5300 to 5900 cm^{-1} region contains only the $^6H_{11/2} \rightarrow {}^6H_{15/2}$ transition, which

allows the ground state splitting to be discerned. Figure 1(a) shows the $^6H_{11/2} \rightarrow {}^6H_{15/2}$ transition of Dy^{3+}; we were able to identify eight peaks in the spectra. Group theory arguments predict J+1/2 doublets (eight peaks) for hexagonal, tetragonal and lower symmetry, whereas cubic symmetry would be expected to give rise to two doublets and three quartets (five peaks) [26]. To verify the identity of the transitions we aligned the $^6H_{11/2} \rightarrow {}^6H_{15/2}$ transition in Fig. 1(a) with the $^6H_{9/2} \rightarrow {}^6H_{15/2}$ and $^6F_{11/2} \rightarrow {}^6H_{15/2}$ mixture of transitions in Fig. 1(b) by means of offsetting the transition energy scale by 1675 cm^{-1}. An additional alignment is found by offsetting Fig. 1(b) by a further 216 cm^{-1}, this should correspond to the separation of the manifolds in the $^6H_{9/2}/{}^6F_{11/2}$ mixed state, although we are unable to ascertain which of these manifolds the alignments in Fig. 1(b) and 1(c) belong to. All the peaks in Fig. 1(a) are aligned with features in the spectra in Figs. 1(b) and 1(c), apart from those at 5733 and 5887 cm^{-1}, the most likely explanation being that these peaks are too weak to be detected. Many extra peaks occur in the $^6H_{9/2}/{}^6F_{11/2} \rightarrow {}^6H_{15/2}$ transition, which could be due to transition from thermally populated higher energy levels, so-called "hot-peaks", in the $^6H_{9/2}/{}^6F_{11/2}$ mixed manifold.

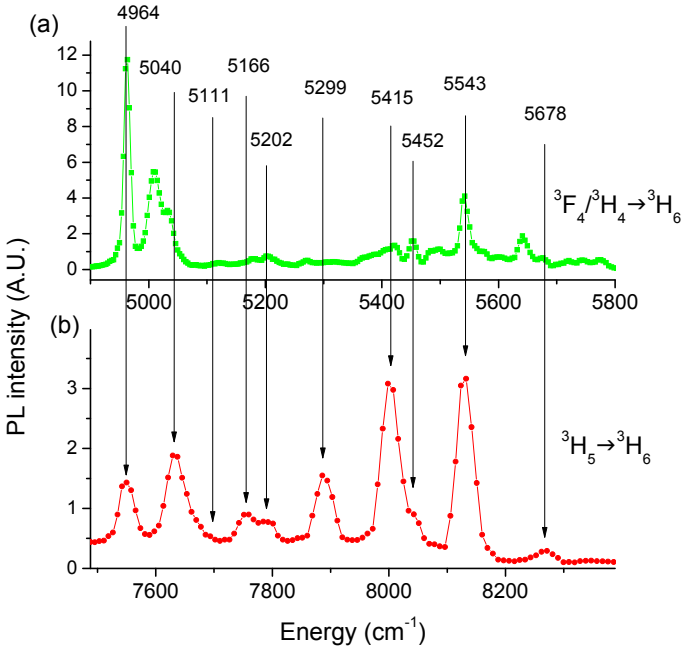

Fig. 2 PL spectra of Tm implanted Si excited at 532 nm. The $^3F_4/^3H_4$ mixed state to the $^3H_6$ ground state transition is shown in (a), the $^3H_5 \rightarrow {}^3H_6$ transition is shown in (b). To align the transition energy scale, (b) is offset from (a) by 2588 cm^{-1}.Peaks identified as corresponding to splitting of the $^3H_6$ ground state are identified with arrows, along with the energy of the peaks.

Figures 2(a) and 2(b) show the PL spectra of Tm implanted Si, similar PL has been reported previously where over 20 transition were identified in the 1.2 to 2.2 µm region (4500-8300 cm^{-1}) [27]. The first excited state of Tm^{3+} is referred to in the literature as either $^3F_4$ or $^3H_4$, [28, 29], but there is no overlap of manifolds, this is purely an issue of nomenclature. The second excited state of Tm^{3+} ($^3H_5$) is an unmixed manifold, therefore the $^3H_5 \rightarrow {}^3H_6$ PL transition can give a clearer picture of the ground state splitting. Comparisons between Figs. 2(a) and 2(b) shows that most of the peaks in the $^3H_5 \rightarrow {}^3H_6$ transition have analogues in the $^3F_4/^3H_4 \rightarrow {}^3H_6$ transition, with the exception of those at 5040 and 5299 cm^{-1}, the most likely explanation being that these peaks are too weak to be detected. Close examination indicates that a kink in Fig. 2(b) corresponds to a small peak in Fig. 2(a) at 5111 cm^{-1}.

3.2 Crystal field parameter fitting

We analysed the splitting of a single J multiplet (the ground state), which was determined from PL spectra, to fit CFPs. The Hamiltonian (H) of a RE in a crystal field can be thought of as consisting of a free ion component (H_F) and a crystal field perturbation (V_{CF})

$$H = H_F + V_{CF} \tag{1}$$

H_F includes Coulomb and spin-orbit interactions, V_{CF} can be thought of as a perturbation generated by the same mechanisms that produce bonding. The multipole expansion of V_{CF} is defined as the linear combination of a set of spherical tensors, $C_q^{(k)}$, and B_q^k which are structural factors referred to as the crystal field parameters which represent the symmetry of the environment [30]

$$V_{CF} = \sum_{k,q} B_q^k C_q^{(k)} \tag{2}$$

As such, crystal field contributions can be built from a superposition of contributions from the individual ligands. Using the triangular relationship of the so-called 3*jm* symbols which describe the coupling of angular momenta, the possible values for rank *k* crystal field operators are restricted to 0, 1, 2, 3, 4, 5 and 6. Hermiticy and time-reversal invariance allow only even rank *k* operators. Since rank $k = 0$ does not produce any crystal field splitting, only rank $k = 2$, 4 and 6 are considered for CFP analysis [31]. To fit CFPs to our experimental data requires the calculation of energy levels from an initial estimate of CFPs. To construct the energy matrix for this calculation, the 3*jm* symbols $\begin{pmatrix} J & k & J' \\ -M_J & q & M'_J \end{pmatrix}$ were combined with the reduced matrix elements $\left(f^n \alpha LSJM_J C^{(k)} f^n \alpha' L'S'J'M'_J \right)$ taken from [32] using

$$f^n \alpha LSJM_J \left| C_q^{(k)} \right| f^n \alpha' L'S'J'M'_J = (-1)^{J-M_J} \begin{pmatrix} J & k & J' \\ -M_J & q & M'_J \end{pmatrix} \left(f^n \alpha LSJM_J C^{(k)} f^n \alpha' L'S'J'M'_J \right) \tag{3}$$

This determines the diagonal components of the $C_q^{(k)}$ spherical tensor operator matrix which are combined with the crystal field parameters B_q^k and summed over the *k* values to produce the energy matrix. Diagonalizing this energy matrix returns the energy levels of the J multiplet. In order to fit CFPs we determined CFPs that minimise the sum of squares difference between the calculated and experimental energy levels. To avoid local minima we systematically searched the parameter space with starting values between previously reported maximum and minimum values. Each site symmetry of the RE has its own particular set of non-vanishing CFPs. In order to determine the site symmetry of our REs, we fitted sets of CFPs corresponding to commonly occurring symmetries. The results are shown in Table 1 which shows that the best fit occurs for tetragonal symmetry for both the REs. For cubic symmetry the constraints: $B_4^4 = 5\, B_0^4$ and $B_4^6 = -21\, B_0^6$ applies [33]. In some respects the comparison with cubic symmetry is superfluous because we observed more PL lines in all the REs than would be expected for cubic symmetry. However, the fitted energy levels shown in Figs. 3(a) and 3(b) allowed us to reconfirm that cubic symmetry is unlikely even if there is uncertainty in the position of the PL lines. Orthorhombic and lower symmetries cannot be reliably fitted to the Dy data because there are more crystal field parameters than energy levels. An important test for the validity of fitted crystal field parameters is that they change gradually when progressing through the lanthanide series. This is the case for our fitted tetragonal parameters for Dy and Tm. Table 1 also shows that when comparing CFPs for symmetries other than tetragonal for Dy and Tm, there is no apparent relationship, indicating that these symmetries are not those of the REs. Figures 3(a) and 3(b) show the experimentally

determined energy levels (E_{exp}) along with those determined by fitting sets of CFPs (E_{fit}) corresponding to various symmetries. Comparing these reconfirms that tetragonal symmetry is the best fit for all the REs.

Table 1 fitted crystal field parameters for various symmetries of Dy and Tm implanted Si. Units are cm^{-1}.

Symmetry	RE	B_0^2	B_2^2	B_0^4	B_2^4	B_3^4	B_4^4	B_0^6	B_2^6	B_3^6	B_4^6	B_6^6	σ
trigonal	Dy	251		41		-550		694		-1694		-1177	75
tetragonal	Dy	386		-555			1510	201			863		12
hexagonal	Dy	671		-1808				-1399				0	62
cubic	Dy			-282				68					210
orthorhombic	Tm	462	134	-228	351		580	-1338	379		980	407	57
trigonal	Tm	469		-1082		-1070		-1107		-56		600	61
tetragonal	Tm	99		-796			1098	201			1077		13
hexagonal	Tm	-286		985				-1134				1363	97
cubic	Tm			-79				-82					106

$\sigma = \sqrt{\Sigma(\Delta_i)^2/(L_{obs}-p)}$, $\Delta_i = E_{exp}-E_{fit}$, L_{obs} is the number of lines, p is the number of CFPs

We used the fitted crystal field parameters for tetragonal symmetry to calculate the entire energy level structure of Dy and Tm in Si using Lanthanide [34] software, which is shown up to 10000 cm^{-1} in Fig. 3 (c). The largely host independent free ion parameters were taken from fitted absorption spectra of REs in LaF_3 [35]. The calculated energy levels were in good agreement with the absolute energies of the PL spectra we observed. The splitting of the excited states may be confirmed in the future if and when it becomes possible to measure by absorption or other means.

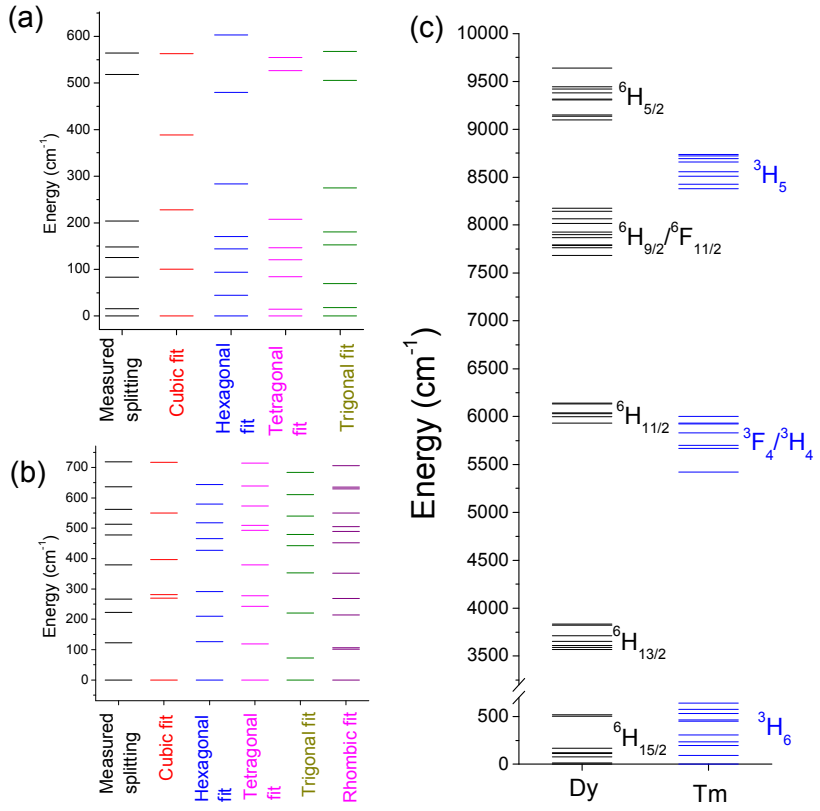

Fig. 3 Comparison of the measured and fitted ground state energy levels for various symmetries for Dy (a), and Tm (b). Calculation the energy level structure of Dy and Tm in Si up to 10000 cm^{-1} using CFPs from the ground state splitting (c).

3.3 Interpretation of crystal field parameters

The CFPs obtained by fitting spectroscopic data are referred to as experimental CFPs and they measure the strength of the interaction between the *f*-shell electrons of lanthanides and their surrounding crystalline environment. However, these parameters do not in themselves give a direct insight into the mechanisms of the crystal field splitting [36]. The rank 4 CFPs are dominated by covalency and closely related overlap contributions [31]. The crystal structure of silicon is the same as that of diamond with tetrahedrally coordinated Si atoms with cubic symmetry and O_h point group and Fd3m space group with a unit cell dimension of 5.431 Å and an equilibrium distance between Si atoms of 2.352 Å. The substitutional site in Si has four nearest neighbours with tetrahedral coordination, the symmetry is nominally cubic, but our CFP fitting shows that the RE has tetragonal symmetry. A tetrahedally coordinated interstitial site also exists in Si, with the same relative position to its four nearest neighbours as the substitutional site. However, the substitutional site has twelve second nearest neighbours with different relative positions to the six second nearest neighbours in the interstitial site. These substitutional and interstitial sites are the only likely sites for the RE in Si, in order to distinguish between these sites and determine their geometry we tested the two electrostatic models illustrated in Figs. 4(a) and 4(b) using a modified version of SIMPRE [37] software. The SIMPRE software uses a point charge electrostatic model in which N ligands are represented by their point charges (Z). The CFPs in Stevens normalisation (A_k^q) are calculated with the following formalism [21, 38]

$$A_k^0 = \frac{4\pi}{2k+1}\sum_{i=1}^{N}\frac{Z_i e^2}{R_i^{k+1}} Z_{k0}(\theta_i,\varphi_i)\, p_{kq} \tag{4a}$$

$$A_k^q = \frac{4\pi}{2k+1}\sum_{i=1}^{N}\frac{Z_i e^2}{R_i^{k+1}} Z_{kq}^c(\theta_i,\varphi_i)\, p_{kq} \qquad (q>0) \tag{4b}$$

$$A_k^q = \frac{4\pi}{2k+1}\sum_{i=1}^{N}\frac{Z_i e^2}{R_i^{k+1}} Z_{k|q|}^c(\theta_i,\varphi_i)\, p_{k|q|} \qquad (q<0) \tag{4c}$$

where R_i, θ_i, and φ_i are the effective polar coordinates of the point charge and Z_i is the effective point charge, associated to the i-th ligand with the RE at the origin; *e* is the electron, p_{kq} are the prefactors of the spherical harmonics and Z_{kq} are the tesseral harmonics expressed in terms of the polar coordinates for the i-th donor atom R_i, θ_i, and φ_i. The Stevens normalisation CFPs (A_k^q) used in Eq. 4(a)-4(c) are related to the Wybourne normalisation CFPs (B_q^k) that we use with the appropriate coefficients [31, 39]. The SIMPRE software does not take into account screening or covalency. However, here we use it to distinguish between a substitutional and an interstitial site, rather than to obtain meaningful structural parameters.

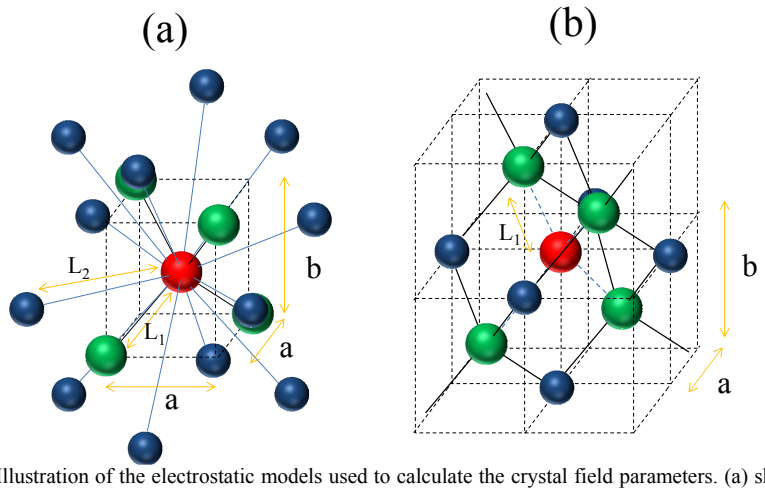

Fig. 4 Illustration of the electrostatic models used to calculate the crystal field parameters. (a) shows a substitutional site in silicon. A rare earth in tetragonal symmetry is shown in red, with four nearest, and twelve second nearest neighbor Si atoms shown in green and blue, respectively. The parameters of the tetragonal primitive cell, *a* and *b*, along with the first and second nearest neighbor distances, L_1 and L_2, respectively are shown. (b) Shows an interstitial site in silicon with the rare earth shown in red. Four nearest neighbor Si atoms are shown in green which have exactly the same relative position to the RE as the substitutional site for the same a and b primitive cell parameters. Six second nearest neighbors are shown in blue, with four at a distance *a* and two at a distance *b* from the RE.

We fitted CFPs calculated by SIMPRE to our experimentally determined CFPs by varying the dimensional parameters, *a* and *b*, of the tetragonal primitive cell and the effective charge (Z) of Si atoms on the RE; if $a \neq b$, the RE has D_{2d} symmetry. The results of the fitting are shown in Table 2 for Dy and Tm implanted Si. CFPs calculated with the substitutional electrostatic model are in relatively good agreement with the experimentally determined CFPs of Dy and Tm with the correct signs and approximately correct relative magnitudes. The point charge electrostatic model fitting accurately predicts the B_0^2 parameter, but overestimates B_0^4, and underestimates the B_4^4, B_0^6 and B_4^6 parameters. The electrostatic model is known to underestimate rank 6 CFPs [40], but this could also be because the point charge electrostatic model is over-simplified for the covalent Si system we are investigating. Therefore, structural parameters calculated from fitting the point charge electrostatic model to our experimental CFPs may be shifted from their true values to mimic the charge distribution in covalent Si [41], but should still be related to the true values. In this respect our fitted structural parameters can be viewed as estimates. The B_0^2 parameter belongs only to the tetragonal component of the crystal field [42], it is therefore dependent on the degree of axial asymmetry i.e. the difference between *a* and *b*, whereas the other parameters are more dependent on the absolute values of *a* and *b* and Z, therefore we can have more confidence in the degree of axial asymmetry than absolute values determined by the point charge electrostatic model. In contrast with the substitutional electrostatic model, the interstitial electrostatic model gives the incorrect sign for B_0^4 in Dy and the incorrect sign for B_0^4 and B_4^4 in Tm, along with a significantly poorer fit, indicated by the σ value. The large difference in Z for Dy and Tm in the interstitial model may also be unphysical. Although the point charge model does not take into account screening or covalency, it does suggest that Dy and Tm exist in the tetrahedrally coordinated substitutional site illustrated in Fig. 4(a). Both Dy and Tm have tetragonal D_{2d} symmetry, however the primitive cell for Dy has significantly higher axial asymmetry than Tm. Our effective charges are comparable with those previously reported: the effective charge

in III-V compounds is 2-2.5 [43], the Mulliken charges of Si atoms in zeolites was found to be ~2.5 [44]. The axial asymmetry could be caused by our dislocation engineering technique which introduces a uniaxial strain field caused by dislocation loops aligned to the four non-parallel <111> lattice planes [1, 45, 46]. Another possibility is the formation of a complex, with axial asymmetry, by charge compensation of the RE^{3+} by other defects such as vacancies or impurities.

Table 2. CFPs from fitted PL lines (exp.), CFPs calculated with the substitutional electrostatic model (SEM), CFPs calculated with the interstitial electrostatic model (IEM) along with parameters of the tetragonal primitive cell, *a* and *b*, the first and second nearest neighbor distances, L_1 and L_2, respectively, and the effective charge (Z)

RE	B_0^2	B_0^4	B_4^4	B_0^6	B_4^6	*a*(Å)	*b*(Å)	L_1(Å)	L_2(Å)	Z	σ
Dy (exp.)	386	-555	1510	201	863						
Dy (SEM)	372	-1087	610	110	249	2.75	2.85	2.41	3.96	2.76	1215
Dy (IEM)	307	320	71	303	365	2.91	2.72	2.47		3.62	1761
Tm (exp.)	99	-796	1098	201	1077						
Tm (SEM)	100	-958	561	102	200	2.75	2.78	2.39	3.91	2.91	1045
Tm (IEM)	67	216	-68	314	545	2.87	2.84	2.48		7.17	1637

The D_{2d} symmetry that we have determined for Dy^{3+} and Tm^{3+} implanted Si does not match the symmetries that we identified as being important for quantum technology applications. These symmetries were C_{3v} symmetry required for the stabilization of the magnetic moment Ho atoms or the D_{4d} symmetry required for increased ground state tunneling gaps. Nevertheless, based on previous work on Er implanted Si, different processing conditions should vary the local environment and symmetry of Dy^{3+} and Tm^{3+} implanted Si, which can we quickly and easily determined by our analysis method. Also, all the RE and symmetry combinations that result in a stabilization of the magnetic moment, as in Ho atoms on a C_{3v} symmetry substrate [19], have not yet been calculated. So there may be different symmetries that result in stabilization of the magnetic moment.

4. Conclusions

We report PL measurement and analysis from multiple J manifolds in Dy and Tm implanted Si. Comparing these manifolds allowed us to identify the ground state splitting with a higher degree of certainty than has been achieved previously. We used this data on the ground state splitting to fit sets of CFPs that correspond to various common symmetries. This allowed us to determine that the symmetry of the Dy and Tm ions in the silicon lattice is tetragonal for both ions. We used our fitted CFPs along with previously published free ion parameters to calculate the splitting of every J manifold of Dy and Tm implanted Si, which we report graphically up to just above the band gap of Si. We used a point charge electrostatic model to fit CFPs to our experimentally determined CFPs using structural models for an interstitial and a substitutional site in Si. This allowed us to determine that both Dy and Tm exist in a tetrahedrally coordinated substitution site with tetragonal symmetry. The degree of tetragonal distortion was significantly higher in Dy compared to Tm. We propose that this distortion is produced by a strain field caused by our dislocation engineering technique. This analysis, which reveals detailed symmetry information on RE implanted Si, could be important for designing ion implantation parameters that lead to systems with long decoherence times which would be valuable for quantum technologies based on RE implanted Si.

Acknowledgments

We acknowledge the European Research Council for financial support under the FP7 for the award of the ERC Advanced Investigator Grant SILAMPS 226470. We would like to thank Dr. Adam Connolly for assistance with the modelling software.